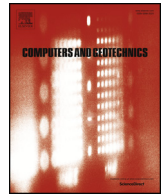




ELSEVIER

Contents lists available at ScienceDirect

Computers and Geotechnics

journal homepage: www.elsevier.com/locate/compgeo

Research Paper

Reseeding of particles in the material point method for soil–structure interactions

Y. Dong

College of Marine Science and Technology, China University of Geosciences, 388 Lumo Road, Wuhan 430074, China

ARTICLE INFO

Keywords:

Material point method
Reseeding
State recovery
Fluctuation mitigation
Split and merge
Soil–structure interaction

ABSTRACT

Lagrangian particles in the material point method (MPM) are free to flow through the background Eulerian mesh to represent material deformation. Excessive compression or tension in the kinematic field tends to entangle the particles from the initial uniform configuration, causing artificial voids or aggregations that lead to loss of the continuity of the stress field and the singular deformation gradient of the particles, undermining computational robustness and accuracy. In this paper, the reseeding operation is performed in elements depending on the numbers of the accommodated particles and their accumulated deformations. The state variables of the reseeded particles are recovered from their surrounding old counterparts. The stresses of the reseeded particles around the structure are adjusted to mitigate the fluctuations of contact force from errors in the state recovery. Benchmark problems of deep penetration of a wished-in-place T-bar and the dynamic impact of a submarine landslide on a partially buried mudmat are analysed. The results of the MPM analyses are validated by comparison with the exact solutions by theoretical analyses and the numerical predictions using computational fluid dynamics (CFD) simulations.

1. Introduction

Large deformation problems are frequently encountered in geotechnical practices, which include the impact of submarine landslides on pipelines (Dong et al. 2017), free-falling torpedo anchors penetrating into seabed (Kim et al. 2018), and the dynamic installation of suction caissons (Cox et al. 2014). To avoid excessive mesh distortion in the simulation of large deformation problems, Lagrangian methods seek to remesh periodically and interpolate field variables from the old meshes to the new ones (Hu and Randolph 1998; Wang et al. 2013; Zhang et al. 2013; Tian et al. 2014); Eulerian methods allow the material to flow through a fixed spatial mesh by decoupling the mesh and material movement (Qiu and Grabe 2012; Zheng et al. 2014); and arbitrary Lagrangian Eulerian (ALE) methods combine the merits of the Lagrangian and Eulerian approaches (Di et al. 2007; Nazem et al. 2008).

The material point method (MPM), originated from the particle-in-cell method in computational fluid dynamics (CFD) (Harlow 1964) and then extended to solid mechanics (Sulsky et al. 1995), falls into the category of the ALE methods. The material in the MPM is represented by a cloud of discrete particles that inherit history-dependent information such as mass, volume, density, velocities, deformation gradients, and stresses. A fixed Eulerian mesh is used to calculate the governing equations in each incremental step without carrying

permanent information. The large deformation of the material can be derived by tracking the particles moving through the background mesh. The MPM has been applied to mimic the flow of granular materials (Bardenhagen et al. 2000), the evolution of subaerial and submarine landslides (Andersen and Andersen 2010; Soga et al. 2016), the dynamic process of pile driving (Hamad 2016), and the large-amplitude displacement of structural elements through soil (Phuong et al. 2016).

However, the large deformation of the material entangles the particles from the initial uniform arrangement, often causing artificial voids among stretched particles or virtual particle aggregations in compressive domains (Ando et al. 2012; Sołowski and Sloan 2015; Yue et al. 2015), somehow similar to mesh distortion in the conventional finite element method (Hu and Randolph 1998; Wang et al. 2013). Also, virtual interpenetration or departure between soil and structure particles may be induced by the ‘penalty’ contact algorithm adopted, although other contact algorithms are also available, such as moving-mesh contact (Ceccato et al. 2016) and generalised frictional contact (Nairn et al. 2018). The varied particle arrangements may introduce numerical noises given the loss of the continuity of the stress field or the singular deformation gradient of the particles. As a result, computational robustness and accuracy tend to be undermined (Steffen et al. 2010). For instance, convergence is not necessarily enhanced with mesh fineness (Liang et al. 2019). Techniques splitting particles in sparse domains and merging particles in dense areas were then developed, Tan

E-mail address: dongyk@cug.edu.cn.

<https://doi.org/10.1016/j.compgeo.2020.103716>

Received 7 January 2020; Received in revised form 4 June 2020; Accepted 20 June 2020

Available online 01 September 2020

0266-352X/ © 2020 Elsevier Ltd. All rights reserved.

and Nairn (2002) and Ma et al. (2009) in the simulation of high-energy explosions as well as Ando et al. (2012), Yue et al. (2015), and Gao et al. (2017) for computer animations. Most of the previous explorations of the rearrangement of particles were based on a qualitative description and limited to visual treatment, which needs to be enhanced for the quantitative analysis of soil–structure interactions in terms of mitigating the fluctuations of contact force.

In this paper, a technique for reseeding particles specialised for soil–structure interactions based on explicit integration is presented. The reseeding operation is performed in elements depending on the number of the accommodated particles and their accumulated deformations. The state variables of the reseeded particles are recovered from their surrounding old counterparts. The stresses of the reseeded particles are adjusted to mitigate the fluctuations of contact force from errors in the state recovery. Then benchmark problems of deep penetration of a wished-in-place T-bar and the dynamic impact of a submarine landslide on a partially buried mudmat are analysed.

2. Algorithm of material point method

2.1. Standard material point method

The standard MPM analyses were undertaken using an in-house program, MPM-GeoFluidFlow, which stems from an open-source package, Uintah (Guilkey et al. 2012), and features a novel contact algorithm ‘Geo-contact’ (Ma et al. 2014), as well as a GPU parallel computing strategy (Dong et al. 2015b; Dong and Grabe 2018). Meshes with identical sizes of square elements were used. The explicit updated Lagrangian calculation in each incremental step was based on the GIMP method presented by Bardenhagen and Kober (2004), while the semi-implicit and implicit integration schemes were presented by Guilkey and Weiss (2003), Sulsky and Kaul (2004), Stomakhin et al. (2013), and Wang et al. (2016). The definition of the stresses and strains followed finite strain theory taking account of the incremental rotation of the configurations between time steps for objectivity: the stresses were measured with the Cauchy stress and updated with the Jaumann rate, and the strains were calculated with the deformation gradient. The main functions within each incremental step for the soil–structure interaction problems are as follows, where the structure is idealised as a rigid body:

(i) The time step starts with the function ‘Initialisation of nodal variables’, initialising the nodal variables of the structure and soil, e.g. masses, velocities, momenta, normal and tangential directions, and internal forces.

(ii) The function ‘Interpolation from particles to nodes’ is to interpolate the masses and momenta of the associated particles (inherited from the previous incremental step) to the nodes

$$m_i = \sum_p S_{ip} m_p \quad (1)$$

$$M_i = \sum_p S_{ip} m_p v_p \quad (2)$$

$$\omega_i^{\text{norm}} = \frac{\sum_p \nabla S_{ip} m_p}{\left\| \sum_p \nabla S_{ip} m_p \right\|} \quad (3)$$

where m_i , M_i , and ω_i^{norm} represent the mass, momentum and normal direction at node i , respectively; m_p and v_p are the mass and velocity of particle p , respectively; S_{ip} and ∇S_{ip} are the shape function and its gradient at node i evaluated at particle p , respectively; and Σ_p represents the summation over all related particles. The derivation of the normal direction ω_i^{norm} in Eq. (3) can be referred to also in Bardenhagen et al. (2000, 2001). For the soil, the internal force is also obtained (while the external nodal force f_i^{ext} will be described at Section 3.4):

$$f_i^{\text{int}} = - \sum_p \nabla S_{ip} \sigma_p V_p \quad (4)$$

where σ_p and V_p are the stress and volume at soil particle p , respectively.

(iii) The function ‘Calculate nodal velocities and accelerations’ is to obtain the velocities and accelerations on the background mesh. At the commencement of the current incremental step, the velocity of the node is

$$v_i = \frac{M_i}{m_i} \quad (5)$$

The acceleration for the soil node from the internal force is

$$a_i = \frac{f_i^{\text{int}} + f_i^{\text{ext}}}{m_i} \quad (6)$$

Then the velocity is updated as

$$v_i' = v_i + a_i \Delta t \quad (7)$$

where Δt is the time increment and determined through the Courant–Friedrichs–Lewy stability condition:

$$\Delta t = \frac{ch}{\sqrt{(\lambda + 2G)/\rho}} \quad (8)$$

where ρ is the soil density, c is the Courant number, h is the size of the square element, and G and λ are Lamé’s parameters.

For the soil node in contact with a moving structure, v_i' is further adjusted into v_i^{new} depending on the adopted contact algorithm ‘Geo-contact’ (Ma et al. 2014), described as follows. Hence, the overall acceleration for the current time step at soil node i is

$$a_i^{\text{new}} = \frac{v_i^{\text{new}} - v_i}{\Delta t} \quad (9)$$

(iv) In the function ‘Update particle state’, the strains of the soil particles are calculated with the deformation gradient using an updated formulation:

$$F_p^{\text{new}} = f_p F_p \quad (10)$$

where f_p is the relative deformation gradient

$$f_p = I + \sum_i \nabla S_{ip} v_i^{\text{new}} \quad (11)$$

with I indicating the identity matrix. The stresses and material properties of the soil particles are calculated using a constitutive model with the deformation rate D_p and vorticity W_p :

$$D_p = \frac{1}{2} \left[\sum_i \nabla S_{ip} v_i^{\text{new}} + \left(\sum_i \nabla S_{ip} v_i^{\text{new}} \right)^T \right] \quad (12)$$

$$W_p = \frac{1}{2} \left[\sum_i \nabla S_{ip} v_i^{\text{new}} - \left(\sum_i \nabla S_{ip} v_i^{\text{new}} \right)^T \right] \quad (13)$$

where the superscript T means the transposition of a tensor. In addition, the velocities and positions are updated by mapping the nodal accelerations and velocities

$$v_p^{\text{new}} = v_p + \sum_i S_{ip} a_i^{\text{new}} \Delta t \quad (14)$$

$$X_p^{\text{new}} = X_p + \sum_i S_{ip} v_i^{\text{new}} \Delta t \quad (15)$$

where X_p represents the particle coordinates at the commencement of the current time step. Essentially, the movement of the particles represents the flow of the soil within the background mesh.

2.2. Contact algorithm

The conventional contact algorithms (Sulsky et al. 1995; York II et al. 2000; Bardenhagen et al. 2000, 2001) were enhanced with an algorithm termed ‘Geo-contact’ (Ma et al. 2014), specialised for soil–structure interaction. Geo-contact introduces a penalty function to the standard multi-field velocity adjustment (Bardenhagen et al. 2000) between the soil and the rigid structure, which is the main reason for the relatively stable reaction forces obtained in this study. Two Eulerian meshes were configured for the soil and structure, respectively, allowing for a multi-valued nodal velocity field. The soil and structure may be in contact at the nodes if both of their mass projections are non-zero values. For a specific node i of the soil in contact, its normal relative velocity to the structure is $\Delta v_i^{\text{norm}} = \Delta v_i \omega_i^{\text{norm}}$, where the relative velocity is $\Delta v_i = (v'_i - v_0)$, with v_0 as the velocity of the structure and v'_i as the updated nodal velocity by Eq. (7). Node i of the soil can be distinguished as approaching or departing from the structure with the relative normal velocity

$$\begin{aligned} \Delta v_i^{\text{norm}} > 0, & \text{ approach} \\ \Delta v_i^{\text{norm}} < 0, & \text{ depart} \end{aligned} \quad (16)$$

The normal contact strategy between the soil and the structure is realised by adjusting the normal relative velocity: (i) for soil node i approaching the structure, the normal relative velocity is eliminated; and (ii) for soil node i departing from the structure, the normal relative velocity is eliminated only if no separation between the structure and the soil is considered (otherwise, the normal relative velocity is maintained). Then the normal contact force at node i is

$$T_i^{\text{norm}} = \frac{m_i \Delta v_i^{\text{norm},*}}{\Delta t} \quad (17)$$

where $\Delta v_i^{\text{norm},*}$ is the adjustment of the normal relative velocity, and the total normal contact force on the structure is

$$T^{\text{norm}} = \sum_i \frac{m_i \Delta v_i^{\text{norm},*}}{\Delta t} \quad (18)$$

In addition to the normal contact constraint, the Geo-contact algorithm also incorporates a tangential constraint along the interface to model a frictional contact condition. The relative tangential velocity of the soil node i to the structure is

$$\begin{aligned} \Delta v_i^{\text{tang}} &= \Delta v_i \omega_i^{\text{tang}} \\ \omega_i^{\text{tang}} &= \omega_i^{\text{norm}} \times \frac{\Delta v_i \times \omega_i^{\text{norm}}}{|\Delta v_i \times \omega_i^{\text{norm}}|} \end{aligned} \quad (19)$$

where ω_i^{tang} is the tangential direction of the interface at node i . Function ‘ \times ’ represents the cross product. The shear along the interface is governed by the Coulomb friction law, i.e. the adjusted tangential relative velocity $\Delta v_i^{\text{tang},*}$ is bounded by $\mu_c \Delta v_i^{\text{norm},*}$, in which μ_c is the Coulomb friction coefficient. In geotechnical applications involving soils with low permeability, a threshold value of the friction stress is usually applied for total stress analyses under undrained conditions:

$$\tau = \alpha \sigma_u \quad (20)$$

where τ is the maximum shear stress along the interface and α is the limiting shear stress ratio, ranging from 0 to 1. So the tangential relative velocity will be adjusted by

$$\Delta v_i^{\text{tang},*} = \min \left(\Delta v_i^{\text{tang}}, \mu_c \Delta v_i^{\text{norm},*}, \frac{\alpha \sigma_u A_i \Delta t}{m_i} \right) \quad (21)$$

where A_i is the interface area represented by node i . If $\Delta v_i^{\text{tang},*} = \Delta v_i^{\text{tang}}$, the sliding material sticks to the structure without slipping, corresponding to the no-slip condition. If $\Delta v_i^{\text{tang},*} = 0$, the smooth condition is considered to allow for free slipping in the tangential direction along the interface; otherwise, the frictional condition is considered. Then the tangential contact force at node i is

$$T_i^{\text{tang}} = \frac{m_i \Delta v_i^{\text{tang},*}}{\Delta t} \quad (22)$$

the total tangential contact force on the structure is

$$T^{\text{tang}} = \sum_i \frac{m_i \Delta v_i^{\text{tang},*}}{\Delta t} \quad (23)$$

and the total contact force is

$$T = T^{\text{norm}} + T^{\text{tang}} \quad (24)$$

However, Equations (18), (23) and (24) tend to predict the contact force with significant fluctuations due to the staggered shapes of the structure defined by structured elements (Ma et al. 2014), which may be solved with unstructured elements (Wang et al. 2017). Another alternative is to introduce a penalty factor β_i to the adjustment of the relative velocity

$$\begin{aligned} \Delta v_i^{\text{adju}} &= \beta_i (\Delta v_i^{\text{norm},*} + \Delta v_i^{\text{tang},*}) \\ \beta_i &= 1 - \left(\frac{\min(s_i, h)}{h} \right)^k \end{aligned} \quad (25)$$

where Δv_i^{adju} is the final adjustment of the nodal velocity, s_i is the distance from node i to the surface of the structure and k is the penalty power. With the introduction of the penalty function, virtual interpenetration and departure between the soil and structure are permitted, which will undermine computational robustness in the simulation of extremely large deformation problems. The excessive interpenetration of the soil particles into the rigid structure caused by continuing compressions, renders the structure essentially permeable; hence, the mass of the soil in the flow field is reduced. A virtual gap can be formed between the departing soil and structure, which means their contact area shrinks inappropriately. Finally the contact force at node i is

$$T_i = \frac{m_i \Delta v_i^{\text{adju}}}{\Delta t} \quad (26)$$

and the total contact force on the structure is

$$T = \sum_i \frac{m_i \Delta v_i^{\text{adju}}}{\Delta t} \quad (27)$$

3. Reseeding technique

3.1. Tracking of soil boundary

The soil domain needs to be outlined before the reseeding of the particles inside. Previous studies include those by Remmerswaal (2017) based on the support domain of particles and Bing et al. (2019) using the B-spline. A new scheme is used here based on the engagement of elements, which are categorised into inner, boundary and outer individuals. An empty element with no particle inside is seen as an outer element. An engaged element is distinguished as inner if all the surrounding elements have particles inside; otherwise, it is recognised as a boundary element. The material boundary lies between the boundary elements and their outer neighbours. Fig. 1(a) illustrates a submarine landslide impacting a partially-buried mudmat, which will be detailed in Section 4.2. Boundary of the sliding mass was detected as in Fig. 1(b) and 1(c). To raise the resolution of the element-based material boundary, the square boundary elements are evenly divided into four lattices. The lattices are also categorised into inner, boundary, and outer individuals. Then the material boundary is drawn along the border between the engaged and empty lattices (Fig. 1(d)). Finally, the obtained saw-tooth-shaped material boundary is cropped along the structure surface if in contact. Although the lattice-based scheme tends to over-estimate the size of the soil domain at free surfaces, the soil–structure interface can be accurately tracked.

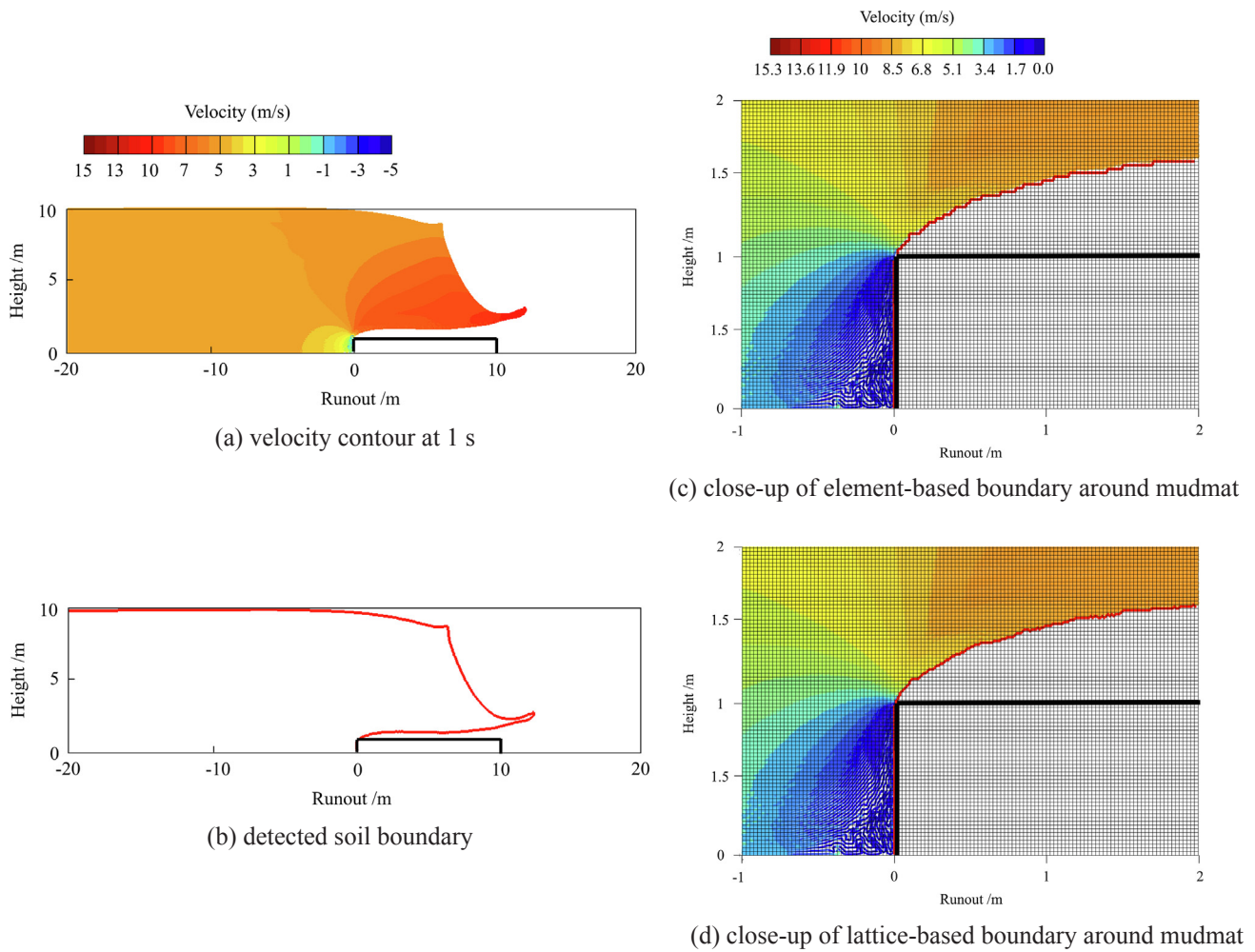


Fig. 1. Tracking of soil boundary for submarine landslide across partially-buried mudmat.

3.2. Reseeding of particles

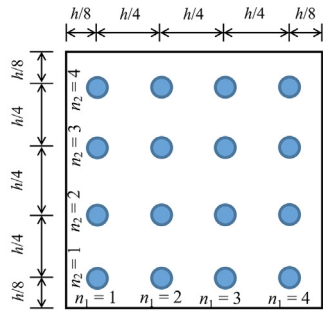
In many cases of MPM analysis, the initial configuration of the four particles in each element is sufficient to present a smooth stress field (Bardenhagen and Kober 2004), while the arrangement of 16 particles in each element is also adopted in the high-velocity impact of a submarine landslide on subsea structures to reduce the fluctuation of impact forces (Dong et al. 2017). However, the particle numbers in some elements under extremely large deformations often decrease to less than half or increase to more than twofold of the initial numbers. In that case, reseeded the deformed particles into a new uniform configuration is necessary. The reseeded operation is performed in elements with the number of particles $N < \beta_L N^0$ (leading to void) or $N > \beta_U N^0$ (corresponding to aggregate), where β_L and β_U are the lower and upper limit coefficients, respectively, and can be determined through trial calculations; and N^0 is the initial number of particles in an element, which is often chosen as 4 or 16.

The accumulated strain of particle p is calculated with the deformation gradient F_p using Eq. (10). We assume that the material represented by a particle has an initial length in the j th direction as L_j^0 . A rough estimate of the deformed length for particle p in the j th direction is $L_{p,j} = F_{p,jj} L_j^0$, where $F_{p,jj}$ refers to the j th diagonal component of F_p . A more accurate estimate of the deformed shape of the particles can be referred to in the studies of Charlton et al. (2017) and Coombs et al. (2020). The gap between neighbouring particles is proportional to the deformed lengths of the particles (Remmerswaal 2017). Therefore, the reseeded operation is also performed in elements where more than one

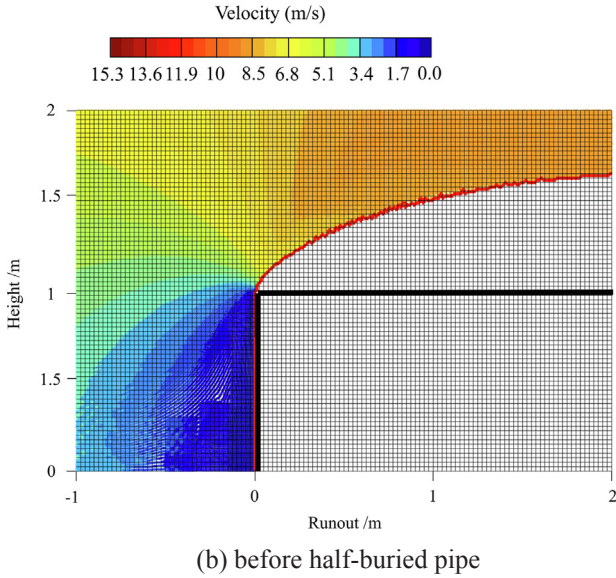
particle has deformed length $L_{p,j} < \beta_L L_j^0$ (i.e. over-compressed, may cause aggregate) or $L_{p,j} > \beta_U L_j^0$ (i.e. over-stretched, may cause void). The new particles are reseeded in the inner and boundary lattices, and the relative coordinates for a reseeded particle r in a lattice are $X_{r,j} = (n_j - 0.5)h/N_j^0$ (see Fig. 2(a)), where N_j^0 , often chosen as two or four, is the initial number of particles in the j th direction in each element; n_j is the sequence number of the reseeded particle in the j th direction and is specified as 1, 2, ..., $N_j^0/2$. Fig. 2(b) shows the reseeded of the particles before a partially-buried mudmat.

3.3. Recovery of state variables

The reseeded particles have an identical density to the old particles because of the consistency of the material. The volumes and masses of the old particles in each element are evenly allocated to the new particles $V_r = \sum_0^N V_p/N^0$, $m_r = \rho V_r$, by which the mass of the material is conserved in each element. The lengths of the particles can then be calculated as $L_{r,j} = \sqrt{V_r}$ in consideration of their square shapes. The deformation gradient F_r is initialised as identity I , which does not affect the following calculation of stress as the updated Lagrangian formulation in Eq. (10) is used. Other state variables, i.e. velocities and stresses, have to be recovered from the old state field. The scheme of recovering from the background mesh, requiring twice the interpolations between the particles and nodes, proves to induce excessive viscosity (Nairn 2015). A feasible scheme is to interpolate the variables from the old configuration of particles to the new ones straightforwardly, similar to the mapping technique used in the large deformation finite element



(a) Particles initialised in an element



(b) before half-buried pipe

Fig. 2. Particles reseeded for submarine landslide across partially-buried mudmat ($N_0 = 16$).

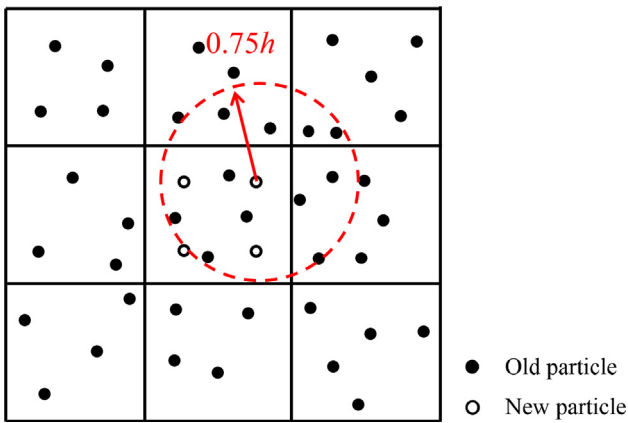
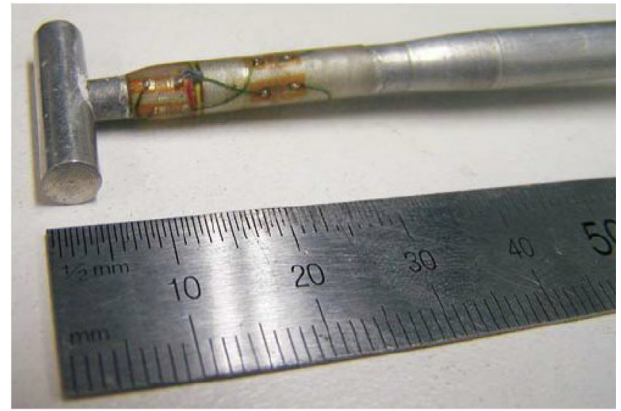


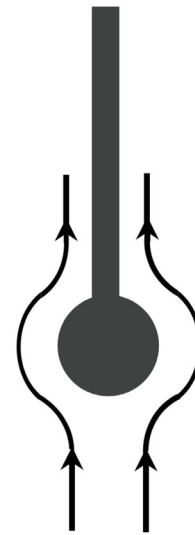
Fig. 3. Recovery of state variables from the surrounding particles.

method (Hu et al. 1998) and the kernel smoothing technique in smoothed particle hydrodynamics (Bui and Nguyen 2017). For a reseeded particle r , all the old particles in its range of $0.75 h$ (Fig. 3), which needs to be sufficiently wide to accommodate more than three old particles, are used to recover the velocities and stresses of the reseeded particles as

$$v_r = \frac{\sum_p d_{rp} v_p}{\sum_p d_{rp}} \quad (28)$$



(a) T-bar



(b) failure mechanism

Fig. 4. Schematic of T-bar (after White et al. 2010).

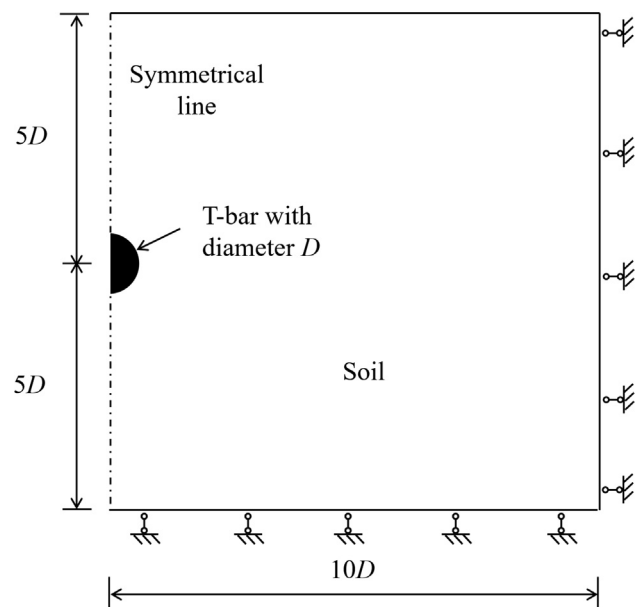


Fig. 5. Schematic for T-bar penetration (non-scaled).

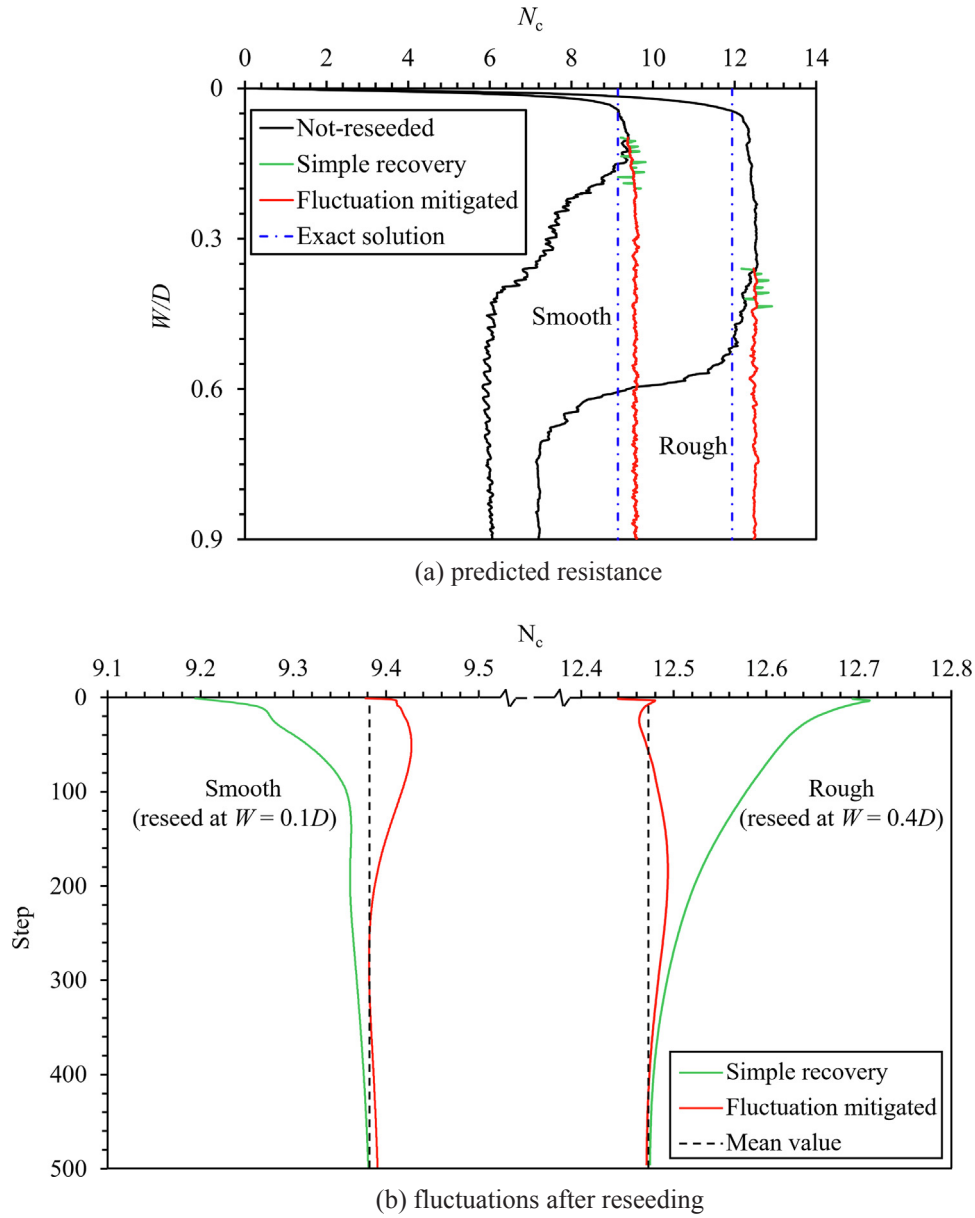


Fig. 6. History of penetration resistance.

$$\sigma_r = \frac{\sum_p d_{rp} \sigma_p}{\sum_p d_{rp}} \quad (29)$$

where d_{rp} is the distance between the reseeded particle r and the old particle p .

Errors are caused due to the difference between the old and new stress fields, which induce virtual accelerations at the surrounding nodes of the new particles. To attenuate the errors and virtual accelerations, the opposite of the old stress field is exerted over the new configuration as a boundary condition in terms of external nodal force $-f_{i,old}^{int}$. The virtual acceleration at node i will be in a form similar to Eq. (6)

$$a_{i,new} = \frac{f_{i,new}^{int} - f_{i,old}^{int}}{m_{i,new}} \quad (30)$$

where $f_{i,new}^{int}$ is the internal forces at node i after reseeding, and $a_{i,new}$ is the virtual acceleration at node i given the difference between the internal and external forces (i.e. unbalanced nodal force; Itasca, 2004;

Charlton et al., 2017). If the nodal acceleration $a_{i,new}$ is being trivial (such as $a_{i,new} \leq 10^{-5} \text{m/s}^2$), the stress field under the new configuration can be seen as equivalent to the old one. Then a number of explicit calculations using Eqs. (7)–(13) can be taken

$$a_{i,new}^n = \frac{f_{i,new}^{int,n} - f_{i,old}^{int}}{m_{i,new}} \quad (31)$$

$$\sigma_r^{n+1} = \Gamma(\sigma_r^n, a_{i,new}^n \Delta t) \quad (32)$$

where the superscript n means the incremental step, the function Γ represents the constitutive model using Eqs. (12) and (13) by replacing $v_{i,j}^{new}$ as $a_{i,new}^n \Delta t$. All the variables in Eqs. (31) and (32) excepting the stress of the new particle σ_r remain unchanged. It should be noted that Eqs. (31) and (32) essentially follow the standard MPM algorithm except for the 'virtual acceleration' used. The accuracy and convergence for the standard MPM algorithm with explicit calculations have been assessed in Wallstedt and Guilkey (2008), Steffen et al. (2008; 2009) and Sołowski and Sloan (2015), which may be inherited here due to the trivial modifications. In Section 4 the convergence will be further

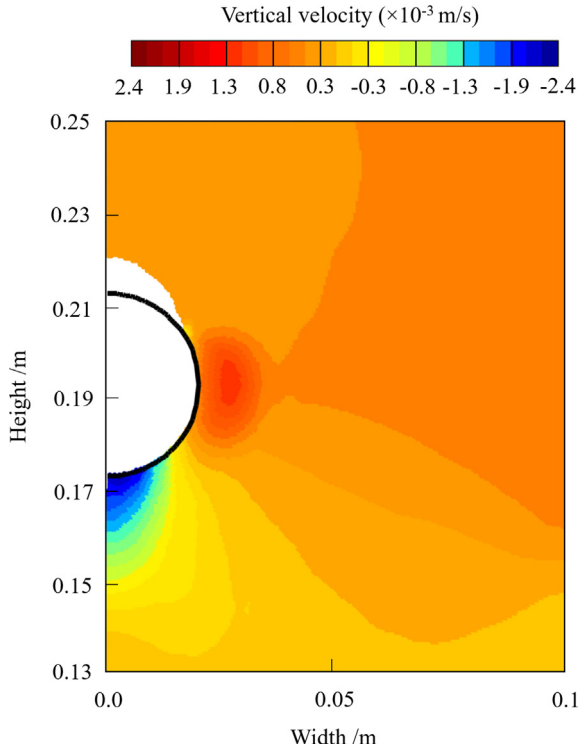


Fig. 7. Virtual gap between structure and above soil.

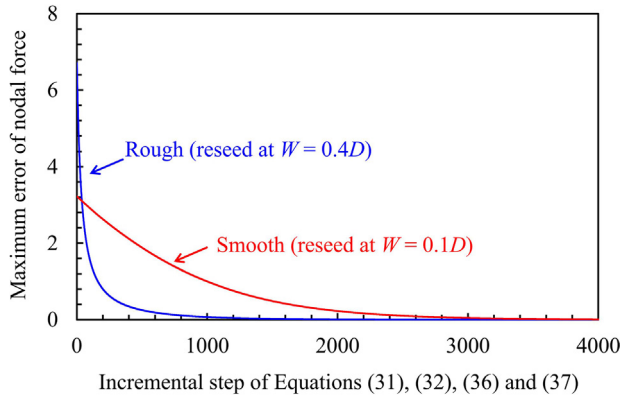


Fig. 8. Mitigation of errors of nodal forces due to particle reseeding around T-bar.

presented for specific benchmark problems.

3.4. Mitigation of contact force fluctuations

The contact force T_i , as described in Section 2.2, is a function of the updated nodal velocities

$$T_i = \frac{m_i \Delta v_i^{\text{adju}}}{\Delta t} = \Phi(v'_i) = \Phi \left(\frac{\sum_r S_{ir} m_r v_r}{\sum_r S_{ir} m_r} + \frac{-\sum_r \nabla S_{ir} \sigma_r V_r \Delta t}{m_i} \right) \quad (33)$$

where Φ represents the contact strategy adopted in the standard MPM algorithm. Errors in the recovery of the state variables, i.e. mass m_r , velocity v_r , volume V_r , and stress σ_r , cause the fluctuation of contact force. The stress σ_r , derived from the nodal velocities, suffers a lower order of accuracy when compared with other variables. Therefore, the fluctuation of contact force is assumed to be mainly caused by the recovery of the stress field. To mitigate the fluctuation of contact force, the stress field represented by the new particles in the contact area

needs to be further adjusted.

The old contact force $T_{i,\text{old}}$ at node i with the old particle configuration can be calculated by following the standard MPM steps (Eqs. (1)–(27)) before the reseeding operation, which can be imposed on the new configuration as an external force. Considering $T_{i,\text{new}} = \frac{m_{i,\text{new}} \Delta v_{i,\text{new}}^{\text{adju}}}{\Delta t}$ in Eq. (33), fluctuation of the contact force in the j th direction can be expressed as

$$T_{i,j,\text{new}} - T_{i,j,\text{old}} = \frac{T_{i,j,\text{new}} - T_{i,j,\text{old}}}{T_{i,j,\text{new}}} \cdot \frac{m_{i,\text{new}} \Delta v_{i,j,\text{new}}^{\text{adju}}}{\Delta t} \quad (34)$$

where $m_{i,\text{new}}$ and $\Delta v_{i,j,\text{new}}^{\text{adju}}$ are the mass and adjusted velocity at node i , respectively, with the new particle configuration. A velocity boundary condition is essentially enforced by the contact force fluctuation as $\frac{T_{i,j,\text{new}} - T_{i,j,\text{old}}}{T_{i,j,\text{new}}} \Delta v_{i,j,\text{new}}^{\text{adju}}$. Then, the stresses of the new particles can be adjusted as

$$\sigma_r^* = \Gamma \left(\sigma_r, \sum_i \frac{T_{i,j,\text{new}} - T_{i,j,\text{old}}}{T_{i,j,\text{new}}} \Delta v_{i,j,\text{new}}^{\text{adju}} \right) \quad (35)$$

where the function Γ represents the constitutive model using Eqs. (12) and (13) by replacing $v_{i,j}^{\text{new}}$ as $\frac{T_{i,j,\text{new}} - T_{i,j,\text{old}}}{T_{i,j,\text{new}}} \Delta v_{i,j,\text{new}}^{\text{adju}}$. In Eq. (35), $T_{i,j,\text{old}}$ is calculated before the reseeding operation, while $T_{i,j,\text{new}}$, σ_r , and $\Delta v_{i,j,\text{new}}^{\text{adju}}$ are obtained based on the new particle configuration. The updated stress σ_r^* is considered to be closer to the original stress field represented by the old particles and hence will cause lower fluctuation of contact force in the j th direction. Then explicit calculations can be performed as follows:

$$T_{i,j,\text{new}}^n = \frac{m_{i,\text{new}} \Delta v_{i,j,\text{new}}^{\text{adju},n}}{\Delta t} = \Phi \left(\frac{\sum_r S_{ir} m_r v_r}{\sum_r S_{ir} m_r} + \frac{-\sum_r \nabla S_{ir} \sigma_r^n V_r \Delta t}{m_i} \right) \quad (36)$$

$$\sigma_r^{n+1} = \Gamma \left(\sigma_r^n, \frac{T_{i,j,\text{new}}^n - T_{i,j,\text{old}}}{T_{i,j,\text{new}}^n} \Delta v_{i,j,\text{new}}^{\text{adju},n} \right) \quad (37)$$

The calculations will be terminated when a sufficiently small difference is reached between $T_{i,j,\text{new}}$ and $T_{i,j,\text{old}}$, i.e. the fluctuation of contact force at node i in the j th direction is mitigated. It should be noted that the mitigation technique using Eqs. (33)–(37), proven to be suitable for simple elasto-plastic constitutive models, needs additional procedures to tackle the complicated constitutive models with a number of history-dependent parameters, such as the SANISAND model (Taiebat and Dafalias, 2008). Admittedly, spurious noise may be caused in the interpolations of the stresses due to complicated stress paths, such as unloading condition, within the elasto-plastic constitutive models, which is not tackled in this study (Hu et al. 1998). Accuracy and viability of the above reseeding operations are validated in the following benchmark analyses.

4. Numerical examples

4.1. Deep penetration of T-bar

For in-situ geotechnical investigation under deep waters, the T-bar (Fig. 4(a)), a penetrometer with no requirement of extra correlation of the penetration resistance by mobilising the full-flow failure mechanism in the surrounding soil (Fig. 4(b)), has been proven to be more accurate than the conventional vane shear test and cone penetration test (Randolph and Houlsby 1984; Einav and Randolph 2005). The shallow penetration of structures (less than half the diameter or width of the structure) has been successfully simulated with the MPM (Dong et al. 2015a, b; Phuong et al. 2016; Ceccato et al. 2017; Wang et al. 2017), while the simulation of deep penetration of the T-bar (close to the diameter) is explored here.

In the analysis, the diameter D of the T-bar was taken as the

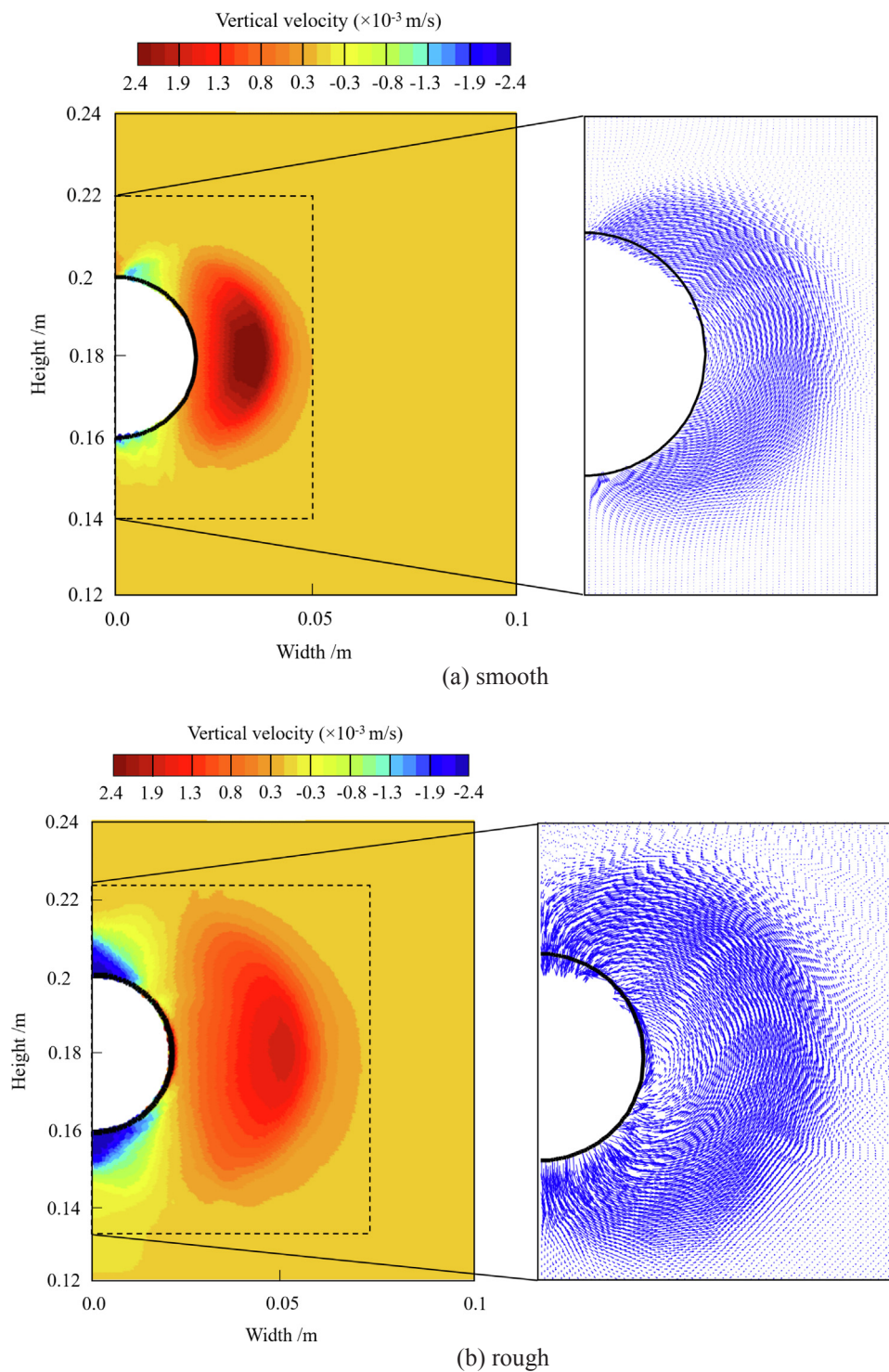


Fig. 9. Full flow of soil mobilised by T-bar (blue arrows describe velocity of particles). (For interpretation of the references to colour in this figure legend, the reader is referred to the web version of this article.)

representative size 0.04 m in the offshore industry, which was simplified as planar to reduce the computational effort. Both the horizontal and vertical dimensions of the soil were $10D$ (Fig. 5), while the T-bar was ‘wished in place’ with an initial embedment depth of $5D$. The element size was selected as $D/40$ (i.e. 0.001 m), which has been validated to be fine enough to reach consistent contact forces with finer elements (Dong et al. 2015a). A 2×2 particle configuration was allocated for each element fully occupied by the soil or T-bar prior to the calculation. In total, 160,000 soil particles were discretised.

The submerged density of the soil was $\rho = 650 \text{ kg/m}^3$. The geostatic stresses induced by the self-weight of the soil was not considered. The soil was modelled as an elastic-perfectly plastic material with the von Mises yield criterion. The homogeneous undrained soil strength was $s_u = 5 \text{ kPa}$. Young’s modulus of the soil was $500s_u$ and Poisson’s ratio was considered as 0.49. To be conservative, the time step Δt was determined through the Courant–Friedrichs–Lewy stability condition with $c = 0.4$ in Eq. (8). The penetration velocity of the T-bar was taken as $0.06D \text{ s}^{-1}$, which is sufficiently slow to investigate the static responses.

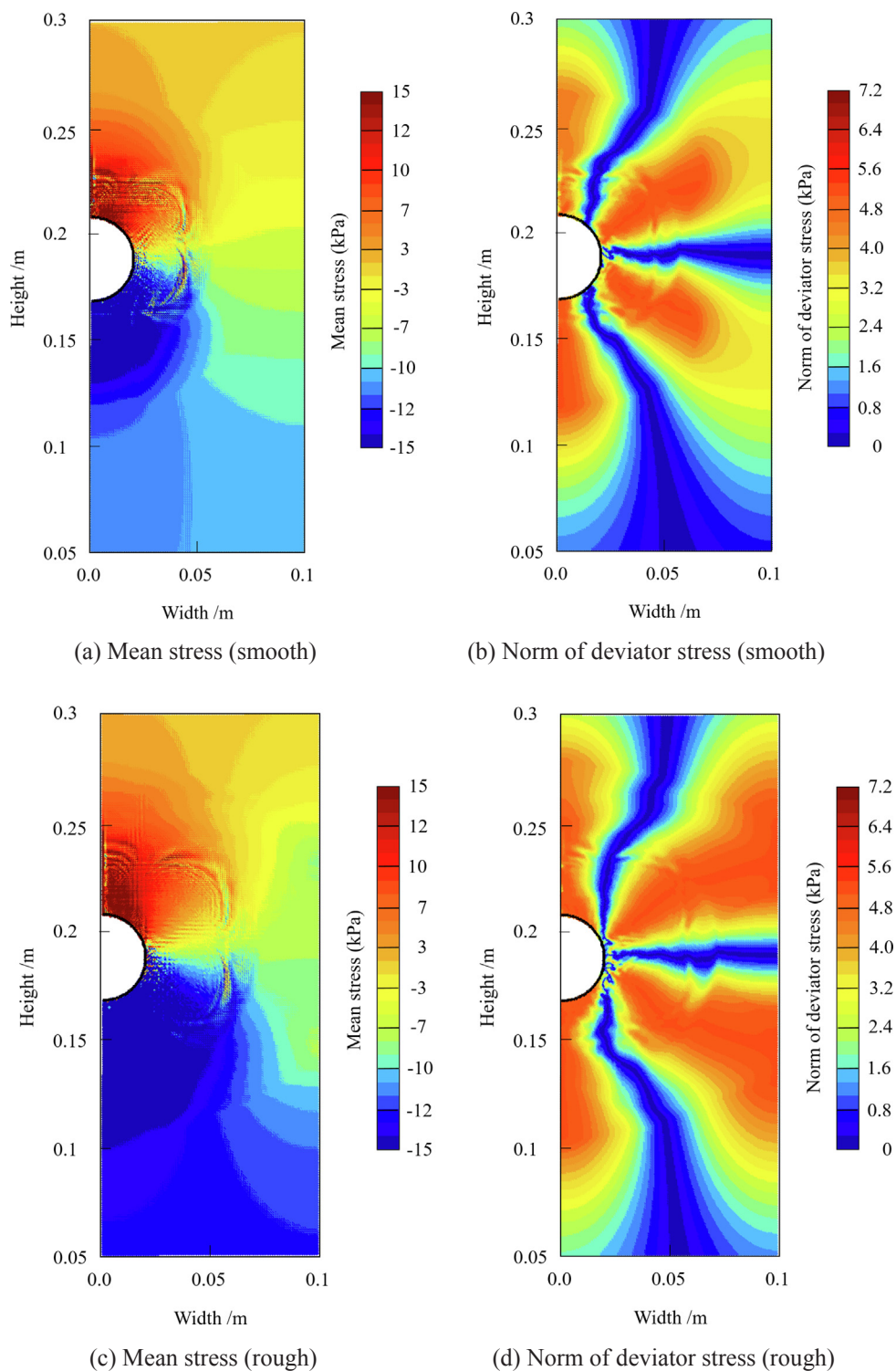


Fig. 10. Stress state around smooth and rough T-bars at 5 s.

The interface between the T-bar and the soil was assumed as fully smooth and fully rough, respectively. Because of the suction generated in the undrained soil behaviour, the soil was enforced to stick to (i.e. no separation) the T-bar after contact. This is critical to the formation of the full-flow failure mechanism in the surrounding soil.

The mobilised soil resistances V are normalised as bearing capacity factors $N_c = V/s_u D$, as shown in Fig. 6(a), with W representing the penetration depth. For the deep penetration of the T-bar mobilising the full flow of the surrounding soil, exact solutions by theoretical analysis

suggest the bearing capacity factor N_c as 9.14 and 11.94, respectively, for fully smooth and rough conditions (Randolph and Houlsby 1984; Einav and Randolph 2005). For the standard MPM analyses without the reseeded procedures, the bearing capacity factors increase quickly to values of 9.38 and 12.52 for the smooth and rough conditions, respectively, close to the exact solutions with convergences less than 5%. In that case, the full-flow failure mechanism of the surrounding soil is mobilised. However, the soil above drops slower than the T-bar given the penalty function in the contact algorithm (Eq. (23)), causing an

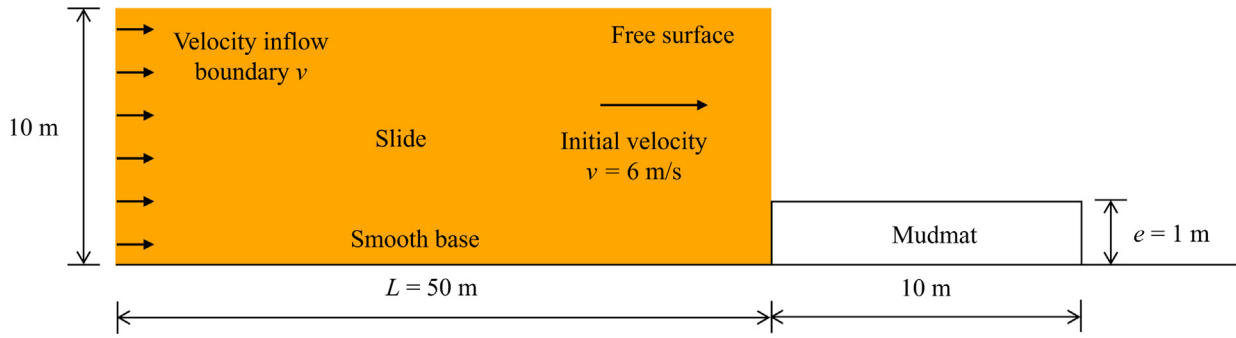


Fig. 11. Schematic for submarine landslide across mudmat (non-scaled).

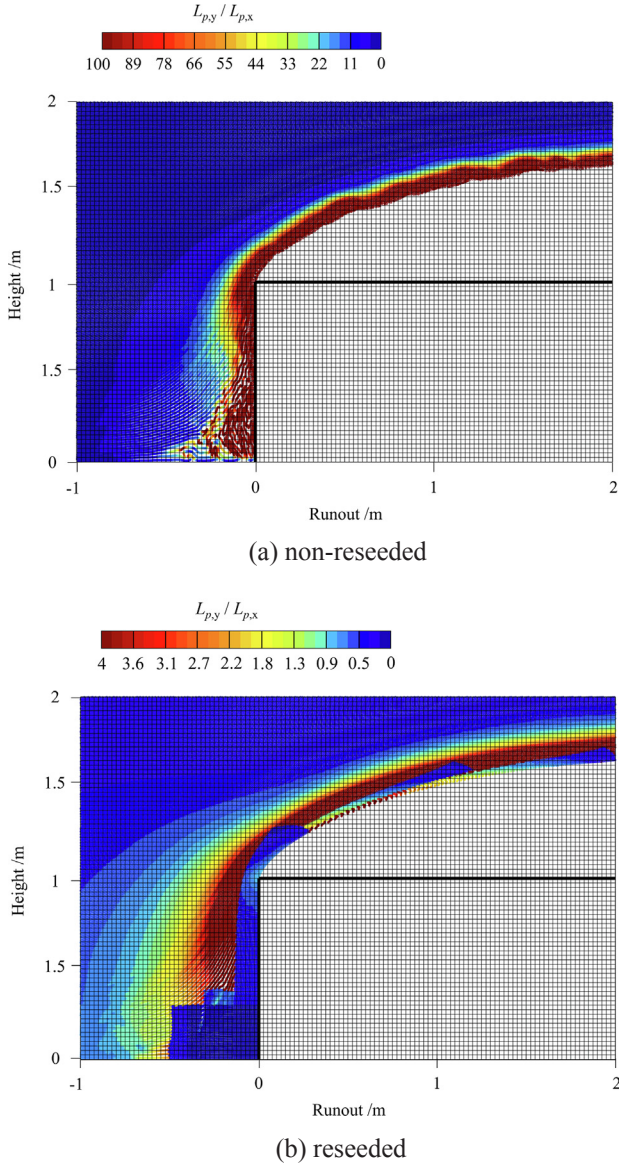


Fig. 12. Particle configurations at 1 s.

essential departure between the soil and T-bar (Fig. 7). The departures occur at a penetration depth of $0.1D$ and $0.36D$ for the smooth and rough conditions, respectively. As a result, the failure mechanism of the soil changes into a partial-flow, and the bearing capacity factors finally reach lower stable values of 6.0 and 7.19 for the smooth and rough conditions, respectively. The bearing capacities of the T-bar with partial-flow in the soil at shallow embedment are further discussed by

White et al. (2010).

The soil particles above the T-bar were then reseeded irregularly to manually compensate the non-trivial departures at $W = 0.1D - 0.2D$ and $W = 0.36D - 0.46D$ for the smooth and rough cases, respectively. The state variables of the new particles were simply recovered from the surroundings as described in Section 3.3, also utilised in the previous studies (Tan and Nairn 2002; Ma et al. 2009; Ando et al. 2012; Yue et al. 2015; Gao et al. 2017). Obvious spurious noises occur in the contact forces immediately after each reseeding operation and last for a number of incremental steps (Fig. 6(a)). Although the noises eventually dissipate, they cause extra complications to the quantitative analysis of the soil–structure interactions, especially when frequent reseedings are required.

Another group of MPM analyses were performed with the mitigations by Eqs. (31), (32), (36) and (37) after the recovery of the particle state. The maximum error of the nodal forces between the old and new configurations is investigated as

$$Error = \text{MAX} \left(\left| \frac{f_{i,\text{new}}^{\text{int},n} - f_{i,\text{old}}^{\text{int}}}{f_{i,\text{old}}^{\text{int}}} \right|, \left| \frac{T_{ij,\text{new}}^n - T_{ij,\text{old}}}{T_{ij,\text{new}}^n} \right| \right). \quad (38)$$

Equilibrium between the configurations can be reached within 4000 steps with the error converges to 10^{-10} (Fig. 8), which implies a satisfying convergence of the mitigation technique using Eqs. (31), (32), (36) and (37). The fluctuations of contact forces ($< 0.4\%$), also partially attributed to the intrinsic errors of the MPM in terms of element crossing and volumetric locking (Coombs et al. 2018), are much smaller than their counterparts with simple-recovery reseedings ($> 2\%$) (Fig. 6(b)). The induced fluctuations can be dissipated in 400 steps. Then the obtained contact forces are relatively stable, and the normalised bearing capacity factors converge to 9.54 and 12.49 for the smooth and rough conditions, respectively (Fig. 6(a)). Because of the reseeding operations, the particles above always stick to the T-bar, and the full-flow mechanism of the surrounding soil is maintained through the whole penetration process (Fig. 9). The stress state around the T-bars at 5 s is shown in Fig. 10.

4.2. Submarine landslide impacting mudmat

Submarine landslides, carrying a mixture of soft sediments and water at speeds of up to 20 m/s, often cause devastating harm to subsea structures in their runout paths (Jakob et al. 2012). The MPM is used to simulate the transient process of an idealised submarine landslide running across a fixed mudmat. An initially rectangular planar slide, having a length of 50 m and a height of 10 m, was idealised and placed before the mudmat with a length of 10 m (Fig. 11). The slide was given an initial horizontal velocity $v = 6$ m/s. The seabed was idealised as smooth in consideration of the low shear resistance because of the hydroplaning effect (De Blasio et al. 2004), which is the key factor for the longer runout distances of the subaqueous slides than their sub-aerial counterparts. A velocity inflow boundary condition was enforced

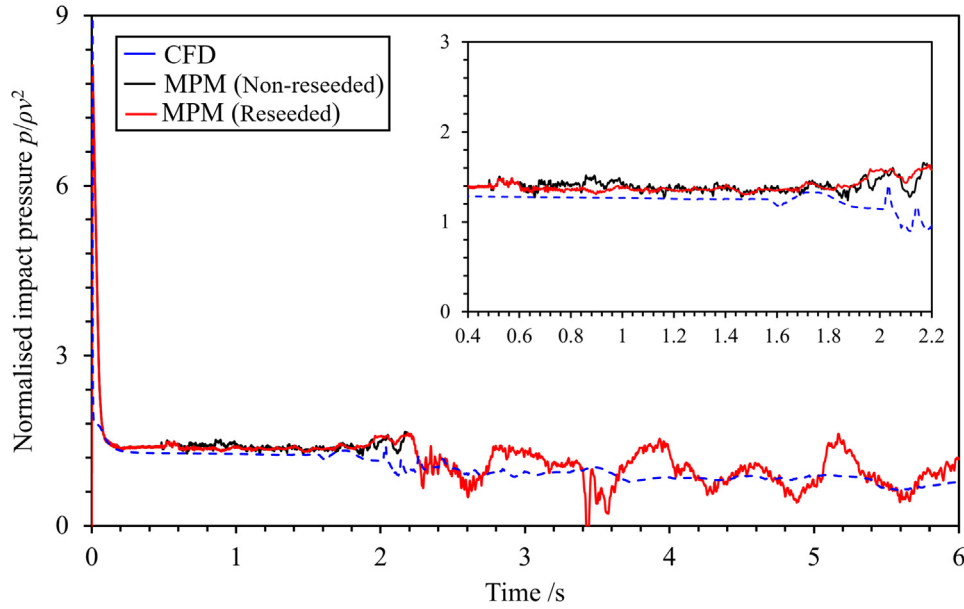


Fig. 13. Normalised impact pressures predicted by CFD and MPM simulations.

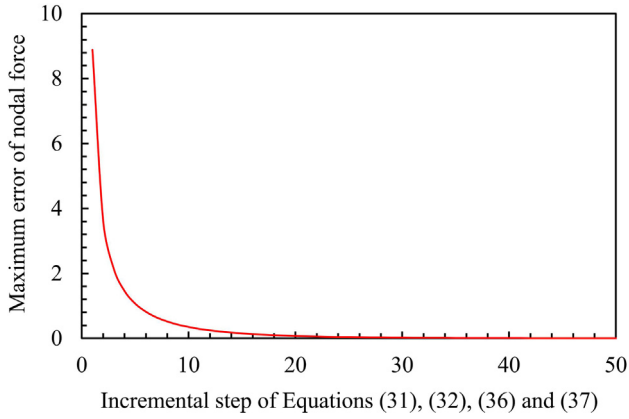


Fig. 14. Mitigation of errors of nodal forces due to particle reseeding around mudmat.

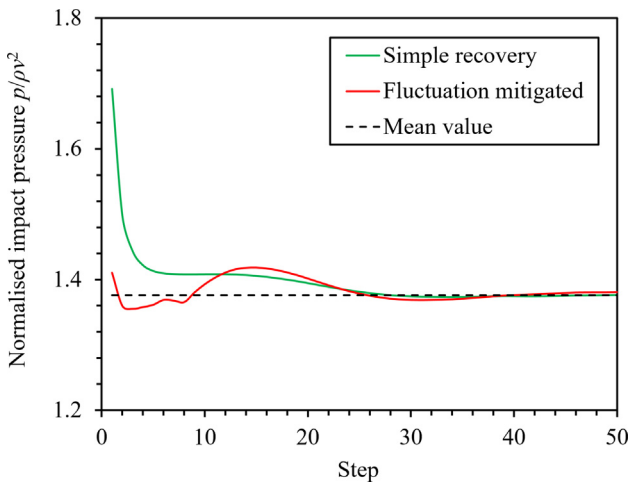


Fig. 15. Dispersion of fluctuations after reseeding particles in submarine landslide.

at the left end of the slide, while its upper and right surfaces were free. Absorbing boundary conditions were added at the left inflow and upper free surfaces to attenuate the out-going stress waves induced by the slide–mudmat impact, which would be detailed in an accompanying paper (Shan et al. 2020). The mudmat was partially buried and exposed to the sliding mass with a height e of 1 m. The mudmat was regarded as smooth, and separation was permitted between the slide and mudmat.

The apparent density of the slide was $\rho = 1,500 \text{ kg/m}^3$. The gravitational acceleration was $g = 9.81 \text{ m/s}^2$. Considering buoyancy, the effective unit weight of the slide material was $(\rho - \rho_w)g$. The rate-dependent undrained shear strength of the non-Newtonian sliding material was characterised by the Herschel–Bulkley (H–B) rheological model (Boukpeti et al. 2012), with $s_{u0} = 0.5 \text{ kPa}$, $\mu = 0.65$, $n = 0.4$, and $\dot{\gamma}_{\text{ref}} = 0.06 \text{ s}^{-1}$:

$$s_u = s_{u0} \left(1 + \mu \left(\frac{\dot{\gamma}}{\dot{\gamma}_{\text{ref}}} \right)^n \right) \quad (39)$$

where s_{u0} is the yield strength at the negligible strain rate, μ the viscosity coefficient, n the ‘shear-thinning’ index, $\dot{\gamma}$ the shear strain rate, and $\dot{\gamma}_{\text{ref}}$ the reference shear strain rate. Equation (39) was incorporated in an elastic–perfectly plastic constitutive model with a von Mises yield surface. For the slide–structure impact problem, a convenient nominal shear strain rate is expressed as $\dot{\gamma} = v/e$ (Dong et al. 2017). The non-Newtonian Reynolds number $R_e = \rho v^2/s_u$ is then 21.2, which is sufficiently small to cause a laminar flow of the slide (Zakeri 2009; Liu et al. 2015). Young’s modulus was taken as a nominal value of $300s_{u0}$. Poisson’s ratio of the slides was taken as 0.49. The time step Δt was determined through the Courant–Friedrichs–Lewy stability condition, with c taken as 0.3 in Eq. (8).

In the MPM analysis, the element size was selected as $e/40$ (i.e. 0.025 m). The mesh independency of the reaction forces on the element size was detailed in an accompanying paper (Dong et al., 2019). A 4×4 particle configuration was allocated for each element fully occupied by the slide or mudmat prior to the calculation, which is to control the noises induced by the particles crossing the element boundaries. In total, 12.8 million slide particles were configured. The robustness of the solid-only MPM was validated by comparison with two-phase computational fluid dynamics (CFD) simulations obtained using a commercial finite volume method package FLUENT (ANSYS, 2011). The settings of the CFD analysis with the void-of-fluid scheme was detailed in Dong’s study (2019).

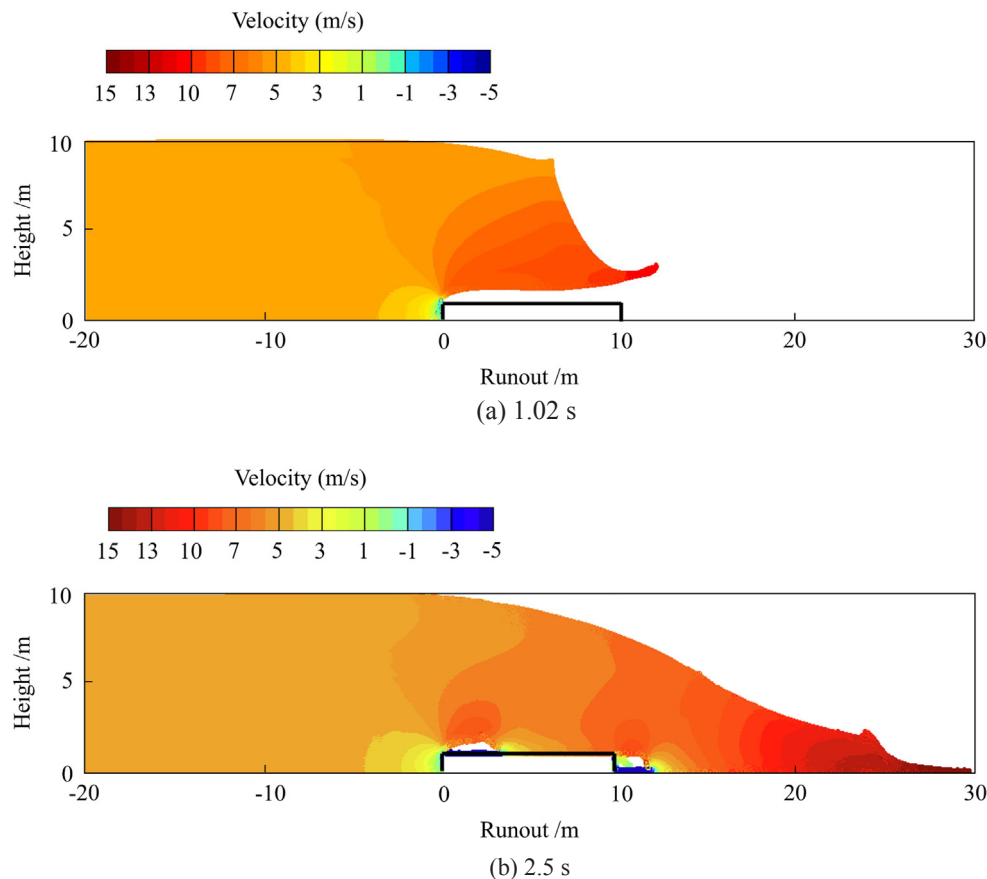


Fig. 16. Velocity contours of slide.

Because of the continuing compressions, the particle configuration of the slide in front of the mudmat is entangled from the initial settings, and the vertical lengths of the particles in front of the mudmat are up to 100 times the horizontal lengths (Fig. 12(a)). As a result, the pressures obtained fluctuate more (Fig. 13), and the computational stability is undermined as the computation is often disrupted by integration errors. Therefore, the non-reseeding MPM analysis was terminated at 2.2 s. Then reseeding operations were performed irregularly over the compression area in front of the mudmat after 0.48 s. With the mitigation technique by Eqs. (36) and (37) along with Eqs. (31) and (32), equilibrium between the configurations can be reached within 50 steps with the error converges to 10^{-10} (Fig. 14), which implies a satisfying convergence. The spurious noises caused by the reseeding procedures are trivial when compared with that using the simple recovery of the particle state (Fig. 15). The induced fluctuations can be dissipated in 30 steps, which converges faster than those in the T-bar cases (400 steps). The main reason may be that more old particles (normally more than 6) in each element are available in the calculations as 16 particles in each element are initialised. The steps required for convergence would vary depending on the specific problems simulated, which can be determined through trial calculations. For the cases in this work, the convergence of the reseeding operations is relatively satisfying. With the reseeding operations, the uniformity of the particle configurations is well maintained, and the ratios of the vertical to horizontal lengths of the particles are maintained below four (Fig. 12(b)). Therefore, the pressures obtained from the reseeding scenario are more stable than those based on the non-reseeded particle configurations.

At the early stage of the impact, the soil flows over the mudmat because of its inertia, shaping a cavity at the top of the mudmat. The flow head falls gradually under the effect of self-weight, and touches the top surface of the mudmat at ~ 1.4 s. Then the flow is separated

into two parts; one part backflows into the cavity, while the other mobilises along the mudmat surface and finally falls onto the base (~ 1.6 s). At the back of the mudmat, another cavity is formed by the backflow of the falling slide (Fig. 16). The average pressures, i.e. the horizontal impact force divided by the projected area of the mudmat, predicted by the MPM are close to the CFD predictions before 1.6 s. After 1.6 s, the pressures are decreased by the backflows in the cavities. The MPM predictions present periodical fluctuations, with the soil in the cavity approaching and departing from the wall of the mudmat. In comparison, the CFD predictions are relatively smooth as the flow field in the cavity characterised by the two-phase mixture of soil and air is more continuous. In general, the pressures after 1.6 s by the CFD analysis are similar to the mean values of their MPM counterparts. Stress state in sliding material at 2.5 s is shown in Fig. 17.

5. Conclusions

A technique for reseeding particles in an entangled arrangement was presented, specialised for soil–structure interactions. The reseeding operation was performed in inner lattices, i.e. quarter elements, depending on the number of accommodated particles and their deformed lengths. The state variables of the reseeded particles were recovered from their original neighbours. The stresses of the reseeded particles around the structure were adjusted to reduce the errors in the new stress field and hence mitigate the fluctuation of contact forces. The penetration of a wished-in-place T-bar for almost one diameter was analysed. With the reseeding operation of the soil particles above the T-bar, the soil was always stuck to the T-bar, and the full-flow mechanism of the surrounding soil was maintained throughout the whole penetration process. The normalised bearing capacity factors converged to 9.54 and 12.49 for the smooth and rough conditions, respectively, close

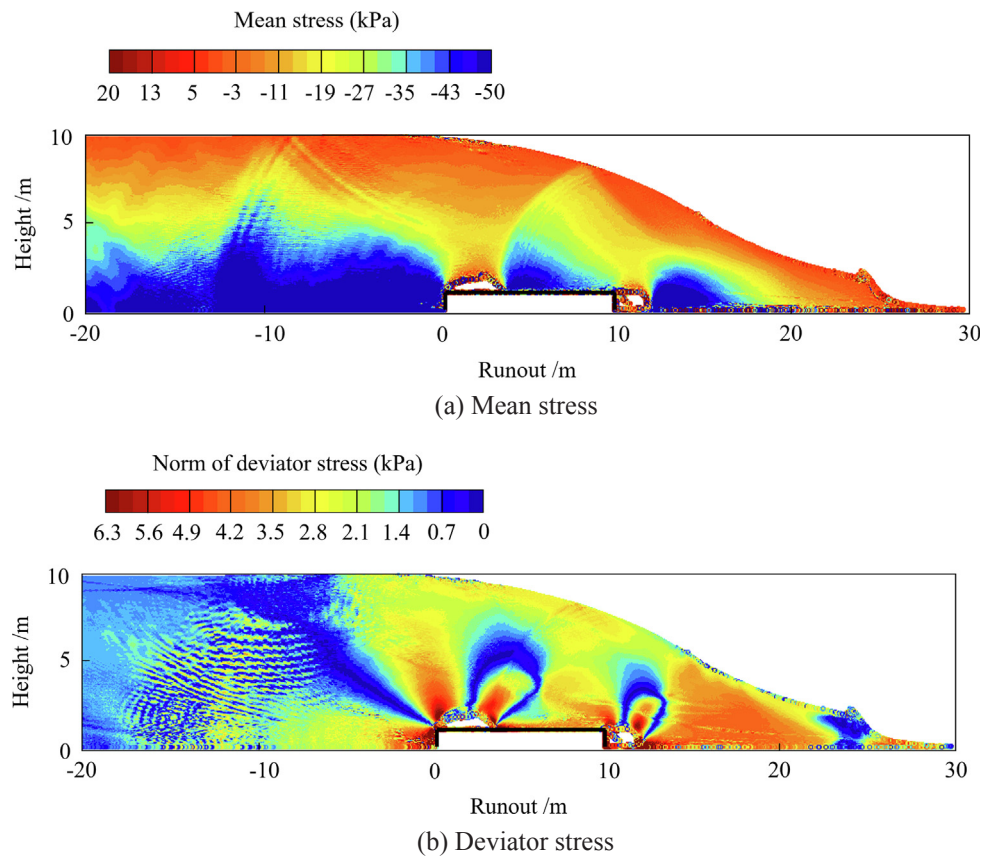


Fig. 17. Stress state in sliding material at 2.5 s.

to the exact solutions of 9.14 and 11.94. Then the transient process of a submarine landslide impacting a partially embedded mudmat was modelled. The Herschel–Bulkley rheological model was incorporated to reflect the dependence of the undrained shear strength of the sliding material on the shear strain rate. With the reseeding operations, the uniformity of the particle configurations was well maintained. The pressures obtained from the reseeding scenario were more stable than those based on the non-reseeded particle configurations. The pressures predicted by the MPM analysis were validated with those predicted by computational fluid dynamic simulations. The reseeding technique would be effective for soil–structure interactions based on explicit integration, which may be easily extended to structure–soil–water interactions with minor modifications. For the MPM algorithms using implicit integrations, applicability of the technique was not explored. Effectiveness of the mitigation technique could also be limited by the complicated constitutive models with a number of history-dependent parameters.

CRediT authorship contribution statement

Y. Dong: Conceptualization, Methodology, Validation, Formal analysis, Writing - original draft, Writing - review & editing.

Declaration of Competing Interest

The authors declare that they have no known competing financial interests or personal relationships that could have appeared to influence the work reported in this paper.

Acknowledgements

This paper was supported by the National Natural Science

Foundations of China (Grant No. 51909248) and the Open Research Fund of State Key Laboratory of Geomechanics and Geotechnical Engineering, Institute of Rock and Soil Mechanics, Chinese Academy of Sciences (Grant No. Z018011).

This work was also supported by the NVIDIA Corporation with the donation of the GPUs Geforce Titan Xp and GeForce Titan V.

The author would also like to acknowledge the valuable input of Profs. Mark Randolph and Yuxia Hu at the University of Western Australia as well as Prof. Dong Wang at Ocean University of China through personal communications.

References

- Andersen, S., Andersen, L., 2010. Modelling of landslides with the material-point method. *Comput. Geosci.* 14 (1), 137–147.
- Ando, R., Thürey, N., Tsuruno, R., 2012. Preserving fluid sheets with adaptively sampled anisotropic particles. *IEEE Trans. Visualization Comput. Graphics* 18 (8), 1202–1214.
- ANSYS. (2011). ANSYS FLUENT 14.0 theory guide, ANSYS, Inc. v.14.0.1.
- Bardenhagen, S.G., Brackbill, J.U., Sulsky, D., 2000. The material-point method for granular materials. *Comput. Methods Appl. Mech. Eng.* 187 (3–4), 529–541.
- Bardenhagen, S.G., Guilkey, J.E., Roessig, K.M., Brackbill, J.U., Witzel, W.M., 2001. An improved contact algorithm for the material point method and application to stress propagation in granular material. *Comput. Modeling Eng. Sci.* 2 (4), 509–522.
- Bardenhagen, S.G., Kober, E.M., 2004. The generalized interpolation material point method. *Comput. Modeling Eng. Sci.* 5 (6), 477–496.
- Bing, Y., Cortis, M., Charlton, T.J., Coombs, W.M., Augarde, C.E., 2019. B-spline based boundary conditions in the material point method. *Comput. Struct.* 212, 257–274.
- Boukpeti, N., White, D.J., Randolph, M.F., 2012. Analytical modelling of a submarine slide under steady flow in relation to the impact load on a pipeline. *Géotechnique* 62 (2), 137–146.
- Bui, H.H., Nguyen, G.D., 2017. A coupled fluid-solid SPH approach to modelling flow through deformable porous media. *Int. J. Solids Struct.* 125, 244–264.
- Ceccato, F., Beuth, L., Simonini, P., 2016. Analysis of piezocone penetration under different drainage conditions with the two-phase material point method. *J. Geotech. Geoenviron. Eng.* 142 (12), 04016066.
- Ceccato, F., Beuth, L., Simonini, P., 2017. Adhesive contact algorithm for MPM and its application to the simulation of cone penetration in clay. *Procedia Eng.* 175, 182–188.

- Charlton, T.J., Coombs, W.M., Augarde, C.E., 2017. iGIMP: An implicit generalised interpolation material point method for large deformations. *Comput. Struct.* 190, 108–125.
- Cox, J.A., O'Loughlin, C.D., Cassidy, M., Bhattacharya, S., Gaudin, C., Bienen, B., 2014. Centrifuge study on the cyclic performance of caissons in sand. *International Journal of Physical Modelling in Geotechnics* 14 (4), 99–115.
- Coombs, W.M., Charlton, T.J., Cortis, M., Augarde, C.E., 2018. Overcoming volumetric locking in material point methods. *Comput. Methods Appl. Mech. Eng.* 333, 1–21.
- Coombs, W.M., Augarde, C.E., Brennan, A.J., Brown, M.J., Charlton, T.J., Knappett, J.A., Ghaffari Motlagh, Y., Wang, L., 2020. On Lagrangian mechanics and the implicit material point method for large deformation elasto-plasticity. *Comput. Methods Appl. Mech. Eng.* 358, 112622.
- De Blasio, F.V., Engvik, L., Harbitz, C.B., Elverhøi, A., 2004. Hydroplaning and submarine debris flows. *J. Geophys. Res.* 109 (C1), 1–15.
- Di, Y., Yang, J., Sato, T., 2007. An operator-split ALE model for large deformation analysis of geomaterials. *Int. J. Numer. Anal. Meth. Geomech.* 31, 1375–1399.
- Dong, Y., Ma, J., Wang, D., Randolph, M.F., 2015a. Assessment of applicability of the material point method in offshore geotechnical engineering. *Comput. Methods Recent Adv. Geomech.* 117–122.
- Dong, Y., Wang, D., Randolph, M.F., 2015b. A GPU parallel computing strategy for the material point method. *Comput. Geotech.* 66, 31–38.
- Dong, Y., Wang, D., Randolph, M.F., 2017. Investigating of impact forces on pipeline by submarine landslide using material point method. *Ocean Eng.* 146, 21–28.
- Dong, Y., Grabe, J., 2018. Large scale parallelisation of the material point method with multiple GPUs. *Comput. Geotech.* 101, 149–158.
- Dong, Y., Wang, D., Randolph, M.F., 2019. Investigating of impact forces on mudmat by submarine landslide using material point method. *Appl. Ocean Res.*, (Under review).
- Einav, I., Randolph, M.F., 2005. Combining upper bound and strain path methods for evaluating penetration resistance. *Int. J. Numer. Meth. Eng.* 63 (14), 1991–2016.
- Gao, M., Tampubolon, A.P., Jiang, C., Sifakis, E., 2017. An adaptive generalized interpolation material point method for simulating elastoplastic materials. *ACM Trans. Graphics* 36 (6), 223.
- Guilkey, J.E., Weiss, J.A., 2003. Implicit time integration for the material point method: quantitative and algorithmic comparisons with the finite element method. *Int. J. Numer. Meth. Eng.* 57 (9), 1323–1338.
- Hamad, F., 2016. Formulation of the axisymmetric CPDI with application to pile driving in sand. *Comput. Geotech.* 74, 141–150.
- Harlow, F.H., 1964. The particle-in-cell computing method for fluid dynamics. *Methods Comput. Phys.* 3 (3), 319–343.
- Hu, Y., Randolph, M.F., 1998. A practical numerical approach for large deformation problems in soil. *Int. J. Numer. Anal. Meth. Geomech.* 22 (5), 327–350.
- Itasca Consulting Group, Inc. (2004) *FLAC3D User Manual: Version 5.0 USA*.
- Jakob, M., Stein, D., Ulmi, M., 2012. Vulnerability of buildings to debris flow impact. *Nat. Hazards* 60 (2), 241–261.
- Kim, Y.K., Hossain, M.S., Lee, J.K., 2018. Dynamic installation of a torpedo anchor in two-layered clays. *Can. Geotech. J.* 55 (3), 446–454.
- Liang, Y., Zhang, X., Liu, Y., 2019. An efficient staggered grid material point method. *Comput. Methods Appl. Mech. Eng.* 352, 85–109.
- Liu, J., Tian, J., Yi, P., 2015. Impact forces of submarine landslides on offshore pipelines. *Ocean Eng.* 95, 116–127.
- Ma, J., Wang, D., Randolph, M.F., 2014. A new contact algorithm in the material point method for geotechnical simulations. *Int. J. Numer. Anal. Meth. Geomech.* 38 (11), 1197–1210.
- Ma, S., Zhang, X., Lian, Y., Zhou, X., 2009. Simulation of high explosive explosion using adaptive material point method. *Comput. Model. Eng. Sci.* 39 (2), 101–123.
- Nairn, J.A., 2015. Numerical simulation of orthogonal cutting using the material point method. *Eng. Fract. Mech.* 149, 262–275.
- Nairn, J.A., Bardenhagen, S.G., Smith, G.D., 2018. Generalized contact and improved frictional heating in the material point method. *Computat. Particle Mech.* 5, 285–296.
- Nazem, M., Sheng, D., Carter, J.P., Sloan, S.W., 2008. Arbitrary Lagrangian-Eulerian method for large-strain consolidation problems. *Int. J. Numer. Anal. Meth. Geomech.* 32, 1023–1050.
- Phuong, N.T.V., Van Tol, A.F., Elkadi, A.S.K., Rohe, A., 2016. Numerical investigation of pile installation effects in sand using material point method. *Comput. Geotech.* 73, 58–71.
- Qiu, G., Grabe, J., 2012. Numerical investigation of bearing capacity due to spudcan penetration in sand overlying clay. *Can. Geotech. J.* 49 (12), 1393–1407.
- Randolph, M.F., Houlsby, G.T., 1984. The limiting pressure on a circular pile loaded laterally in cohesive soil. *Géotechnique* 34 (4), 613–623.
- Remmerswaal, G., 2017. Development and implementation of moving boundary conditions in the Material Point Method (Doctoral dissertation). Retrieved from < <https://repository.tudelft.nl/islandora/object/uuid:d5d89599-1e45-4ac1-b966-49a1a785a350?collection=education> > .
- Shan, Z., Dong, Y., Wang, D., Zhang, A., 2020. Implementation of absorbing boundary conditions in dynamic simulation of the material point method. *Géotechnique Letters* (To submit).
- Soga, K., Alonso, E., Yerro, A., Kumar, K., Bandara, S., 2016. Trends in large-deformation analysis of landslide mass movements with particular emphasis on the material point method. *Géotechnique* 66 (3), 248–273.
- Sołowski, W.T., Sloan, S.W., 2015. Evaluation of material point method for use in geotechnics. *Int. J. Numer. Anal. Meth. Geomech.* 39 (7), 685–701.
- Steffen, M., Kirby, R.M., Berzins, M., 2008. Analysis and reduction of quadrature errors in the material point method (MPM). *Int. J. Numer. Meth. Eng.* 76 (6), 922–948.
- Steffen, M., Kirby, R.M., Berzins, M., 2010. Decoupling and balancing of space and time errors in the material point method (MPM). *Int. J. Numer. Meth. Eng.* 82 (10), 1207–1243.
- Stomakhin, A., Schroeder, C., Chai, L., Teran, J. and Selle, A. (2013). A material point method for snow simulation. *ACM Trans. Graphics (TOG)*, 32(4), 102, 1-9.
- Sulsky, D., Kaul, A., 2004. Implicit dynamics in the material-point method. *Comput. Methods Appl. Mech. Eng.* 193 (12), 1137–1170.
- Sulsky, D., Zhou, S.J., Schreyer, H.L., 1995. Application of a particle-in-cell method to solid mechanics. *Comput. Phys. Commun.* 87 (1), 236–252.
- Tan, H., Nairn, J.A., 2002. Hierarchical, adaptive, material point method for dynamic energy release rate calculations. *Comput. Methods Appl. Mech. Eng.* 191, 2095–2109.
- Taiebat, M., Dafalias, Y.F., 2008. SANISAND: Simple anisotropic sand plasticity model. *Int. J. Numer. Anal. Meth. Geomech.* 32 (8), 915–948.
- Tian, Y., Cassidy, M.J., Randolph, M.F., Wang, D., Gaudin, C., 2014. A simple implementation of RTSS and its application in large deformation analysis. *Comput. Geotech.* 56, 160–167.
- Wallstedt, P.C., Guilkey, J.E., 2008. An evaluation of explicit time integration schemes for use with the generalized interpolation material point method. *J. Comput. Phys.* 227 (22), 9628–9642.
- Wang, L., Coombs, W. M., Augarde, C. E., Brown, M., Knappett, J., Brennan, A., Richards, D. and Blake, A. (2017). Modelling screwpile installation using the MPM, in Rohe, A., Soga, K., Teunissen, H. and Coelho, B.Z. eds, 175: 1st International Conference on the Material Point Method (MPM 2017). Delft, Netherlands, Elsevier, 124-132.
- Wang, D., Randolph, M.F., White, D.J., 2013. A dynamic large deformation finite element method based on mesh regeneration. *Comput. Geotech.* 54, 192–201.
- Wang, B., Vardon, P.J., Hicks, M.A., 2016. Investigation of retrogressive and progressive slope failure mechanisms using the material point method. *Comput. Geotech.* 78, 88–98.
- White, D., Gaudin, C., Boylan, N., Zhou, H., 2010. Interpretation of T-bar penetrometer tests at shallow embedment and in very soft soils. *Can. Geotech. J.* 47 (2), 218–229.
- York II, A.R., Sulsky, D., Schreyer, H.L., 2000. Fluid - membrane interaction based on the material point method. *Int. J. Numer. Meth. Eng.* 48 (6), 901–924.
- Yue, Y., Smith, B., Batty, C., Zheng, C., Grinspun, E., 2015. Continuum foam: a material point method for shear-dependent flows. *ACM Trans. Graphics* 34 (5), 160.
- Zakeri, A., 2009. Submarine debris flow impact on suspended (free-span) pipelines: Normal and longitudinal drag forces. *Ocean Eng.* 36 (6), 489–499.
- Zhang, X., Krabbenhoft, K., Pedroso, D.M., Lyamin, A.V., Sheng, D., Vicente da Silva, M., Wang, D., 2013. Particle finite element analysis of large deformation and granular flow problems. *Comput. Geotech.* 54, 133–142.
- Zheng, J., Hossain, M.S., Wang, D., 2014. Numerical modeling of spudcan deep penetration in three-layer clays. *Int. J. Geomech.* 15 (6), 04014089.